The Astrophysical Journal, 569:349–361, 2002 April 10
© 2002. The American Astronomical Society. All rights reserved. Printed in U.S.A.

COLLAPSE OF A ROTATING SUPERMASSIVE STAR TO A SUPERMASSIVE BLACK HOLE: POST-NEWTONIAN SIMULATIONS

Motoyuki Saijo,[1] Thomas W. Baumgarte,[1,2] Stuart L. Shapiro,[1,3] and Masaru Shibata[4]
Received 2001 October 16; accepted 2001 December 18

ABSTRACT

We study the gravitational collapse of a rotating supermassive star by means of a $(3 + 1)$ hydrodynamic simulation in a post-Newtonian approximation of general relativity. This problem is particularly challenging because of the vast dynamic range in space that must be covered in the course of collapse. We evolve a uniformly rotating supermassive star from the onset of radial instability at $R_p/M = 411$, where R_p is the proper polar radius of the star and M is the total mass-energy, to the point at which the post-Newtonian approximation breaks down. We introduce a scale factor and a "comoving" coordinate to handle the large variation in radius during the collapse ($8 \lesssim R_p/M_0 \lesssim 411$, where M_0 is the rest mass) and focus on the central core of the supermassive star. Since T/W, the ratio of the rotational kinetic energy to the gravitational binding energy, is nearly proportional to $1/R_p$ for an $n = 3$ polytropic star throughout the collapse, the imploding star may ultimately exceed the critical value of T/W for dynamic instability to bar-mode formation. Analytic estimates suggest that this should occur near $R_p/M \sim 12$, at which point $T/W \sim 0.27$. For stars rotating uniformly at the onset of collapse, however, we do not find any unstable growth of bars prior to the termination of our simulation at $R_p/M_0 \sim 8$. We do find that the collapse is likely to form a supermassive black hole coherently, with almost all of the matter falling into the hole, leaving very little ejected matter to form a disk. In the absence of nonaxisymmetric bar formation, the collapse of a uniformly rotating supermassive star does not lead to appreciable quasi-periodic gravitational wave emission by the time our integrations terminate. The coherent nature of the implosion, however, suggests that rotating supermassive star collapse will be a promising source of gravitational wave bursts. We also expect that, following black hole formation, long-wavelength quasi-periodic waves will result from quasi-normal ringing. These waves may be detectable by the Laser Interferometer Space Antenna.

Subject headings: gravitation — gravitational waves — hydrodynamics — instabilities — relativity — stars: rotation

1. INTRODUCTION

There is increasing evidence that supermassive black holes (SMBHs) exist at the center of all galaxies and that they are the sources that power active galactic nuclei and quasars (Rees 1998; Macchetto 1999). For example, VLBI observations of the Keplerian disk around an object in NGC 4258 indicate that the central object has a mass $M \sim 3.6 \times 10^7\ M_\odot$ and radius of less than $\sim$13 pc. Also, large numbers of observations are provided by the *Hubble Space Telescope* (*HST*) suggesting that SMBHs exist in galaxies such as M31 ($3 \times 10^7\ M_\odot$), M87 [$(1\text{–}2) \times 10^9\ M_\odot$] and our own Galaxy ($2.5 \times 10^6\ M_\odot$) (see, for example, Macchetto 1999 for a brief overview).

Although evidence of the existence of SMBHs is compelling, the actual formation process of these objects is still uncertain (Rees 2001). Several different scenarios have been proposed, some based on stellar dynamics, others on gas hydrodynamics, and still others that combine the processes. In one stellar dynamic scenario, a dense star system composed of compact stars becomes dynamically unstable to a collisionless, relativistic radial mode and undergoes catastrophic collapse to an SMBH (Zeldovich & Podurets 1965; Shapiro & Teukolsky 1985a, 1985b; Quinlan & Shapiro 1987). In an alternative scenario, massive stars build up within a dense cluster following collisions and mergers of ordinary stars. After repeated collisions and mergers, supermassive stars (SMSs) are formed, and these become unstable to a hydrodynamic, relativistic radial mode (Iben 1963; Chandrasekhar 1964a, 1964b; J. Feynman, unpublished, as quoted in Fowler 1964) and eventually collapse to form SMBHs (Lee 1987; Quinlan & Shapiro 1990; Ebisuzaki et al. 2001). In still another scenario, massive halos of self-interacting dark matter in the early universe undergo the gravothermal catastrophe (secular core collapse), followed by catastrophic collapse to SMBHs once their cores become relativistic (Balberg, Shapiro, & Inagaki 2002; Balberg & Shapiro 2002). In a typical gas hydrodynamic scenario, a contracting primordial gas cloud builds up sufficient radiation pressure to inhibit fragmentation and the gas directly builds up an SMS (Sanders 1970; Begelman & Rees 1978; Haehnelt, Natarajan, & Rees 1998). Some mass inevitably will be shed, but most of the matter is trapped during the ensuing gravitational collapse, forming an SMBH. At present, there is no definitive observation as yet that confirms or rules out any one of these scenarios.

Here we focus on the collapse of an SMS. Baumgarte & Shapiro (1999) investigated the equilibrium, stability, and quasi-static evolution of an SMS with uniform rotation. During quasi-static evolution, uniform rotation can be maintained by either internal viscosity or magnetic braking. They showed that the nondimensional ratios R_p/M, T/W,

[1] Department of Physics, University of Illinois at Urbana-Champaign, Urbana, IL 61801-3080.
[2] Department of Physics and Astronomy, Bowdoin College, 8800 College Station, Brunswick, ME 04011-8488.
[3] Department of Astronomy and NCSA, University of Illinois at Urbana-Champaign, Urbana, IL 61801.
[4] Graduate School of Arts and Sciences, University of Tokyo, Komaba, Meguro, Tokyo 153-8902, Japan.

and J/M^2 for all critical configurations at the onset of collapse are universal numbers, independent of the history or mass of the star. Here, R_p is the proper polar radius, M is the gravitational mass (total mass-energy), T is the rotational kinetic energy, W is the gravitational binding energy, and J is the angular momentum. They also pointed out the possibility of bar formation during catastrophic collapse prior to black hole (BH) formation, assuming that the collapse is nearly homologous ($T/W \propto 1/R_p$). They provided a crude analytic argument suggesting that the imploding star should pass the dynamic bar-mode instability point $T/W \sim 0.27$ at the radius $R_p/M \sim 12$, but were not able to assess the consequences of this fact. New & Shapiro (2001) later investigated the quasi-static evolution of an SMS with differential rotation, assuming negligible viscosity and magnetic fields. They showed that in this case, bar formation prior to the onset of relativistic instability is inevitable.

One of the primary observational missions for space-based detection of gravitational waves is the investigation of supermassive objects (Thorne 1998). Since the Laser Interferometer Space Antenna (LISA) will have long arms (10^6 km), the detector will be most sensitive in the low-frequency band (10^{-4} to 10^{-1} Hz). Potential sources of high signal-to-noise ratio events in this frequency range include quasi-periodic waves arising from nonaxisymmetric bars in collapsing SMSs and the inspiral of binary SMBHs. In addition, the nonspherical collapse of rotating SMSs to SMBHs could be a significant source of burst and quasi-normal ringing radiation. In this paper, we track the collapse of an SMS by numerical simulation to investigate some of these possibilities.

The growth of bars during the catastrophic collapse of stars has been studied previously for scenarios leading to core bounce, such as in supernova core collapse. Rampp, Müller, & Ruffert (1998) employed a two-component equation of state with an effective adiabatic index larger than 4/3, which causes bounce. They concluded that the star forms a bar in several dynamic timescales after it exceeds the critical value for dynamic bar-mode instability ($T/W \gtrsim 0.27$ for Newtonian incompressible equilibrium stars). Since the rotating core reexpands after the bounce and T/W falls to a lower value $\lesssim 0.27$, however, the nonaxisymmetric instability does not have sufficient time to enter the nonlinear regime, and the bar does not grow. Therefore, gravitational radiation is not generated effectively in this core bounce. Brown (2001) considered the same problem but chose a different equation of state to allow the star more time (by a factor of 100) to reside in the unstable regime $T/W \gtrsim 0.27$. Nevertheless, he too found that the dynamic instability was too weak to produce an appreciable bar and a large emission of gravitational waves. No one has considered the growth of bars during collapse without a bounce, which is the case for an SMS where the adiabatic index is close to 4/3.

We take our initial stellar model to be a marginally unstable SMS star near the critical point, $R_p/M \sim 430$. We treat the gas adiabatically, since for sufficiently massive stars neither photon nor neutrino losses are dynamically significant (Linke et al. 2001). We take the adiabatic index to be 4/3, appropriate for a radiation pressure–dominated SMS, and construct a critical, uniformly rotating polytrope with index $n \approx 3$ for our starting point. Our goal is to determine the final outcome of the collapse. We want to address the following questions: does an SMBH definitely form following the catastrophic collapse? Is the collapse coherent or does the central region collapse first, followed by the gradual accretion of the envelope? Does the collapsing configuration fragment? Does a disk form? Does a rotating bar form during the collapse?

We use a post-Newtonian (PN) hybrid hydrodynamic code in $(3 + 1)$ dimensions to track SMS collapse. Our adopted hybrid scheme is relativistically exact for static spherical spacetimes (Shibata, Baumgarte, & Shapiro 1998). The onset of radial instability occurs when $T/W \ll 0.1$, so our initial equilibrium spacetime is very nearly spherical. Locating the onset of radial instability in an SMS requires the presence of nonlinear gravitation to at least 2PN order (Zeldovich & Novikov 1967; Baumgarte & Shapiro 1999). For these reasons, the nonlinearity captured in our hybrid scheme, which extends beyond 1PN, is essential to treat this problem. Of course, it is necessary to use a fully general relativistic code to follow the final implosion of the matter into a BH and to reliably determine the gravitational waveforms. [Shapiro & Teukolsky (1979) followed SMS collapse in full general relativity for a nonrotating configuration with a spherical $(1 + 1)$ code.] However, a fully relativistic $(3 + 1)$ code capable of handling the large dynamic range spanned by SMS collapse is not yet available. Fortunately, since our initial configuration is nearly Newtonian, we can use our hybrid scheme to track most of the implosion up to the point where the formation of a BH is likely. Our hybrid scheme is also adequate to address most of the questions raised above, at least in a preliminary fashion.

This paper is organized as follows. In § 2, we present the basic equations of our PN formulation in comoving coordinates. We demonstrate the ability of our code to distinguish stable from unstable stars in § 3. We discuss our numerical results for catastrophic collapse in § 4. In § 5, we summarize our findings. Throughout this paper, we use geometrized units ($G = c = 1$) and adopt Cartesian coordinates (x, y, z) with the coordinate time t. Greek and Latin indices run over (t, x, y, z) and (x, y, z), respectively.

2. NUMERICAL METHOD AND KEY EQUATIONS

In this section, we briefly derive the $(3 + 1)$ hybrid PN relativistic hydrodynamic equations (Shibata, Oohara, & Nakamura 1997; Shibata, Baumgarte, & Shapiro 1998) in comoving coordinates. We solve the fully relativistic equations for hydrodynamics, but neglect some higher order dynamic PN terms in the Einstein field equations. Note that this approximation gives the exact solution for a static spherical spacetime. To track the collapse over the vast dynamic range from $\gtrsim 410M$ down to a few M and to investigate the central core at late times, we require a suitable comoving coordinate system. Such a coordinate choice is possible because in Newtonian gravity, an $n = 3$ spherical polytrope collapses homologously (Goldreich & Weber 1980). This special behavior does not strictly hold in general relativity (Shapiro & Teukolsky 1979), nor does it apply to a rotating configuration, but it holds approximately for much of the implosion of a critical SMS configuration, since it is nearly Newtonian and slowly rotating. Therefore, we can construct a comoving frame, subtracting the mean "Hubble" flow from the local velocity, to follow most of the collapse with sufficient grid resolution.

First, we construct a PN metric in the comoving frame. The line element in the PN formalism is written as (Chan-

drasekhar 1965; Blanchet, Damour, & Schäfer 1990)

$$ds^2 = g_{\mu\nu}dx^\mu dx^\nu = (-\alpha^2 + \beta_k\beta^k)dt^2 + 2\beta_k dx^k dt + \psi^4\delta_{ij}dx^i dx^j , \quad (1)$$

where α, β^i, and ψ are lapse function, shift vector, and conformal factor, respectively. Therefore, as in the study of BH formation in the Friedmann universe (Shibata & Sasaki 1999), we define the comoving frame by

$$x^i = \hat{a}\hat{x}^i , \quad (2)$$

where $\hat{x}^i$ is the spatial coordinate in the comoving frame and $\hat{a}$ is a scale factor that only depends on t. Hereafter, $\hat{A}$ will represent the quantity A as measured in comoving coordinates. Note that we do not change the time coordinate. We write the PN line element in comoving coordinates as

$$ds^2 = \hat{g}_{\mu\nu}d\hat{x}^\mu d\hat{x}^\nu = (-\hat{\alpha}^2 + \hat{\beta}_k\hat{\beta}^k)dt^2 + 2\hat{\beta}_k d\hat{x}^k dt + \hat{a}^2\hat{\psi}^4\delta_{ij}d\hat{x}^i d\hat{x}^j . \quad (3)$$

By matching the two line elements (eqs. [1] and [3]) and using equation (2), we identify

$$\hat{\alpha} = \alpha , \quad (4)$$

$$\hat{\beta}^k = \frac{\beta^k}{\hat{a}} + H\hat{x}^k , \quad (5)$$

$$\hat{\psi} = \psi , \quad (6)$$

where $H \equiv \dot{\hat{a}}/\hat{a}$. Note that among the geometric quantities, we only need to adjust the shift vector.

For a perfect fluid, the energy-momentum tensor in comoving coordinates is written as

$$\hat{T}_{\mu\nu} = \rho\left(1 + \epsilon + \frac{P}{\rho}\right)\hat{u}_\mu\hat{u}_\nu + P\hat{g}_{\mu\nu} , \quad (7)$$

where ρ, ϵ, and P are rest mass density, specific internal energy density, and pressure, respectively. We adopt a Γ-law equation in the form $P = (\Gamma - 1)\rho\epsilon$ in this paper.

In the comoving frame, the continuity equation, energy equation, and Euler equation with Γ-law equation of state including artificial viscosity are written as

$$\frac{\partial(\hat{a}^3\rho_*)}{\partial t} + \frac{\partial}{\partial\hat{x}^i}(\hat{a}^3\rho_*\hat{v}^i) = 0 , \quad (8)$$

$$\frac{\partial(\hat{a}^3 e_*)}{\partial t} + \frac{\partial}{\partial\hat{x}^i}(\hat{a}^3 e_*\hat{v}^i) = -\frac{\hat{a}^3}{\Gamma}(\rho\epsilon)^{-1+1/\Gamma}P_{\rm vis}\frac{\partial}{\partial\hat{x}^i}(\alpha\hat{u}^t\psi^6\hat{v}^i) , \quad (9)$$

$$\frac{\partial}{\partial t}(\hat{a}^3\rho_*\tilde{\hat{u}}_i) + \frac{\partial}{\partial\hat{x}^j}(\hat{a}^3\rho_*\tilde{\hat{u}}_i\hat{v}^j) = -\hat{a}^3\alpha\psi^6\frac{\partial}{\partial\hat{x}^i}(P + P_{\rm vis}) - \hat{a}^3\rho_*\alpha\tilde{\hat{u}}^t\frac{\partial\alpha}{\partial\hat{x}^i} + \hat{a}^3\rho_*\tilde{\hat{u}}_j\frac{\partial\hat{\beta}^j}{\partial\hat{x}^i} + 2\hat{a}^3\rho_*\frac{1 + \Gamma\epsilon}{\hat{u}^t\psi}[(\alpha\hat{u}^t)^2 - 1]\frac{\partial\psi}{\partial\hat{x}^i} , \quad (10)$$

where

$$\rho_* = \rho\alpha\hat{u}^t\psi^6 , \quad (11)$$

$$\hat{v}^i = \frac{\hat{u}^i}{\hat{u}^t} , \quad (12)$$

$$e_* = (\rho\epsilon)^{1/\Gamma}\alpha\hat{u}^t\psi^6 , \quad (13)$$

$$\tilde{\hat{u}}^t = (1 + \Gamma\epsilon)\hat{u}^t , \quad (14)$$

$$\tilde{\hat{u}}_i = (1 + \Gamma\epsilon)\hat{u}_i . \quad (15)$$

Following Shibata (1999), we include artificial viscosity in our system as

$$P_{\rm vis} = \begin{cases} C_{\rm vis}\dfrac{\hat{a}^3 e_*^\Gamma}{(\alpha\hat{u}^t\psi^6)^{\Gamma-1}}(\delta\hat{v})^2 , & \delta\hat{v} \le 0 ; \\ 0 , & \delta\hat{v} \ge 0 , \end{cases} \quad (16)$$

with $\delta\hat{v} = 2\delta\hat{x}\hat{\partial}_i\hat{v}^i$, $C_{\rm vis} = 1$, and $\delta\hat{x}$ is the step size of the comoving grid.

Gravitational field equations in the PN approximation are derived from the Hamiltonian constraint, the momentum constraint, and the maximal time-slicing condition (Shibata et al. 1997, 1998). The equations in the comoving frame are written as

$$\hat{\triangle}\psi = -2\pi\hat{a}^2\psi^5\hat{\rho}_{\rm H} , \quad (17)$$

$$\hat{\triangle}(\alpha\psi) = 2\pi\alpha\hat{a}^2\psi^5(\hat{\rho}_{\rm H} + 2\hat{S}) , \quad (18)$$

$$\delta_{ij}\hat{\triangle}\hat{\beta}^j + \tfrac{1}{3}\hat{\partial}_i\hat{\partial}_j\hat{\beta}^j = 16\pi\alpha\hat{J}_i , \quad (19)$$

where $\hat{\rho}_{\rm H} = n_\mu n_\nu\hat{T}^{\mu\nu}$, $\hat{J}_i = -n_\mu\hat{h}_{i\nu}\hat{T}^{\mu\nu}$, $\hat{S} = \hat{h}^i_\mu\hat{h}_{i\nu}\hat{T}^{\mu\nu}$, $n_\mu = (-\alpha, 0, 0, 0)$, $\hat{h}_{\mu\nu} = \hat{g}_{\mu\nu} + n_\mu n_\nu$, and $\hat{\triangle}$ is the flat Laplacian measured in the comoving frame.

We use the asymptotic falloff behavior for metric quantities at large radius in order to set an appropriate boundary condition at the grid edge (Shibata et al. 1998). Only the rescaled shift vector $\hat{\beta}^i$ requires special consideration. Although β^i has a simple falloff at the large radii, falling as $\sim O(r^{-2})$, $\hat{\beta}^i$ diverges as $\sim H\hat{x}^i$. In order to eliminate the divergent behavior of $\hat{\beta}^i$, we introduce a new vector $\hat{W}^i$ as

$$\hat{W}^i \equiv \hat{\beta}^i - H\hat{x}^i . \quad (20)$$

In terms of $\hat{W}^i$, the momentum constraint equation (19) can be rewritten as

$$\delta_{ij}\hat{\triangle}\hat{W}^j + \tfrac{1}{3}\hat{\partial}_i\hat{\partial}_j\hat{W}^j = 16\pi\alpha\hat{J}_i . \quad (21)$$

From a computational point of view, it is useful to split this momentum equation into one vector Poisson equation and one scalar Poisson equation using the technique of Shibata (1997):

$$\delta_{ij}\hat{W}^j = 4\hat{B}_i - \tfrac{1}{2}[\hat{\partial}_i\hat{\chi} + \hat{\partial}_i(\hat{B}_k\hat{x}^k)] , \quad (22)$$

where $\hat{B}_i$ and $\hat{\chi}$ satisfy

$$\hat{\triangle}\hat{B}_i = 4\pi\alpha\hat{J}_i , \quad (23)$$

$$\hat{\triangle}\hat{\chi} = -4\pi\alpha\hat{J}_i\hat{x}^i . \quad (24)$$

We also need to rewrite the Euler equation (eq. [10]) using $\hat{W}^i$ as

$$\frac{\partial}{\partial t}(\hat{a}^2\rho_*\tilde{\hat{u}}_i) + \frac{\partial}{\partial\hat{x}^j}(\hat{a}^2\rho_*\tilde{\hat{u}}_i\hat{v}^j) = -\hat{a}^2\alpha\psi^6\frac{\partial}{\partial\hat{x}^i}(P + P_{\rm vis}) - \hat{a}^2\rho_*\tilde{\hat{u}}^t\frac{\partial\alpha}{\partial\hat{x}^i} + \hat{a}^2\rho_*\tilde{\hat{u}}_j\frac{\partial\hat{W}^j}{\partial\hat{x}^i} + 2\hat{a}^2\rho_*\frac{1 + \Gamma\epsilon}{\hat{u}^t\psi}[(\alpha\hat{u}^t)^2 - 1]\frac{\partial\psi}{\partial\hat{x}^i} , \quad (25)$$

where

$$\hat{v}^i \equiv \frac{\hat{u}^i}{\hat{u}^t} = -(\hat{W}^i + H\hat{x}^i) + \frac{\delta^{ij}\hat{u}_j}{\hat{a}^2\psi^4\hat{u}^t} . \quad (26)$$

The fluid velocities in the two frames are related through

equation (2) by

$$v^i = \hat{a}(\hat{v}^i + H\hat{x}^i)\,. \tag{27}$$

Finally, we must decide how to choose H. As long as homology holds during the collapse, we can always subtract the Hubble flow by choosing the appropriate H ($\hat{v}^r = 0$). This is why the star does not contract during the collapse in the comoving frame. Since rotating collapse does not strictly hold homology because of the effects of rotation and PN gravity, success in exploring the late collapse depends on the location where we choose to subtract the Hubble flow. Although an $n = 3$ polytropic star has a large envelope, most of the mass is located in the central core. Therefore, we set H around the mean radius according to

$$H = \left(-\hat{W}^x + \frac{\delta^{xj}\hat{u}_j}{\hat{a}^2\psi^4\hat{u}^t}\right)\Big/\hat{x}^x\Big|_{\hat{r}\sim\hat{r}_m}\,, \tag{28}$$

where the mean radius is defined as

$$\hat{r}_m = \sqrt{\frac{\int \rho_* \hat{x}^2 d^3\hat{x}}{\int \rho_* d^3\hat{x}}}\,. \tag{29}$$

We experiment by using different radii in the neighborhood of r_m for measuring H, and we choose the one that yields the most accurate evolution. Note that for homologous Newtonian collapse of an $n = 3$ spherical polytrope, H defined above is independent of the radius at which it is evaluated.

We monitor several global quantities of the system during the collapse. The gravitational mass M, rest mass M_0, proper mass M_p, angular momentum J, rotational kinetic energy T, and gravitational binding energy W of the rotating star are defined as

$$\begin{aligned} M &= -\frac{1}{2\pi}\int_{r\to\infty} \nabla^i\psi dS_i \\ &= \int \hat{a}^3\left[(\rho + \rho\epsilon + P)(\alpha\hat{u}^t)^2 - P\right]\psi^5 d^3\hat{x}\,, \end{aligned} \tag{30}$$

$$M_0 \equiv \int \rho u^t\sqrt{-g}d^3x = \int \hat{a}^3\rho_* d^3\hat{x}\,, \tag{31}$$

$$\begin{aligned} M_p &= \int \rho u^t(1+\epsilon)\sqrt{-g}d^3x \\ &= \int \hat{a}^3\rho_*(1+\epsilon)d^3\hat{x}\,, \end{aligned} \tag{32}$$

$$\begin{aligned} J &= \frac{1}{8\pi}\int_{r\to\infty}(xK^i_y - yK^i_x)\psi^6 dS_i \\ &= \int \hat{a}^3(\hat{x}\hat{J}_y - \hat{y}\hat{J}_x)\psi^6 d^3\hat{x}\,, \end{aligned} \tag{33}$$

$$T = \frac{1}{2}\int \Omega dJ = \frac{1}{2}\int \hat{a}^3\hat{\Omega}(\hat{x}\hat{J}_y - \hat{y}\hat{J}_x)\psi^6 d^3\hat{x}\,, \tag{34}$$

$$W = |M_p + T - M|\,, \tag{35}$$

where Ω is the angular velocity of the star:

$$\Omega = \frac{xv^y - yv^x}{x^2 + y^2}\,. \tag{36}$$

Note that in PN gravity, M and J are not strictly conserved, especially when the field becomes strong and higher order corrections to the gravitational field become important. These quantities, however, should be well conserved during those early and intermediate epochs when gravity remains weak. Also, J defined above should be strictly conserved whenever the system is axisymmetric. Since our system is nearly axisymmetry prior to any bar formation, monitoring J conservation enables us to check the accuracy of our numerical results. We also define the quadrupole moment I_{ij} as

$$I_{ij} = \int \hat{a}^5\rho_*\hat{x}^i\hat{x}^j d^3\hat{x} \tag{37}$$

and the nonaxisymmetric distortion parameter η as

$$\eta = \frac{I_{xx} - I_{yy}}{I_{xx} + I_{yy}}\,. \tag{38}$$

We choose a polytropic equation of state for our initial data, with $P = \kappa\rho^{1+1/n}$, where $n \approx 3$ and κ is a constant appropriate for thermal radiation pressure of constant specific entropy (see, e.g., Baumgarte & Shapiro 1999, eq. [3]). For numerical purposes, it is convenient to rescale all quantities with respect to κ. Since $\kappa^{n/2}$ has dimensions of length, we introduce the following nondimensional variables:

$$\begin{aligned} \bar{M} = \kappa^{-n/2}M, \quad R = \kappa^{-n/2}R, \quad \bar{J} = \kappa^{-n}J\,, \\ \bar{\Omega} = \kappa^{n/2}\Omega, \quad \bar{\rho} = \kappa^n\rho\,. \end{aligned} \tag{39}$$

Therefore, our numerical results apply to arbitrary mass, where we simply need to adjust κ according to

$$\frac{M}{10^6\ M_\odot} = \left(\frac{\kappa^{n/2}}{1.48\times 10^6\ \mathrm{km}}\right)\bar{M}\,, \tag{40}$$

to apply our result to arbitrary mass. Henceforth, we adopt nondimensional quantities but omit the bars for convenience. Equivalently, we set $\kappa = 1$.

3. STABILITY ANALYSIS

Before simulating rotating SMS collapse in our comoving scheme, we first assess the stability and accuracy of our $(3+1)$ PN hybrid code. For this purpose, we study the stability of stars along an equilibrium sequence of fixed entropy (fixed κ) using our dynamic code and compare the results with the exact turning point criterion. We recall that the onset of radial instability occurs at the turning point in a plot of M versus ρ_c along the sequence.

3.1. *Spherical Symmetric Case*

In general relativity and PN gravitation, all nonrotating spherical polytropes with index $n = 3$ are radially unstable to collapse and have no turning points along their equilibrium sequences. To test the ability of our code to distinguish stable from unstable spherical stars, we must study polytropes with a slightly smaller n; we set $n = 2.96$ for this purpose, for which the equilibrium structure remains close to that of a radiation pressure–supported SMS. We perturb the initial equilibrium at $t = 0$ by slightly decreasing the pressure and following the subsequent evolution. More specifically, we decrease the pressure constant κ according to $\kappa \to 0.99\kappa$. We use modest grid sizes (typically $99\times 99\times 50$)[5] for this test, covering the star with 81 grid points across its diameter.

[5] Our code has equatorial plane symmetry.

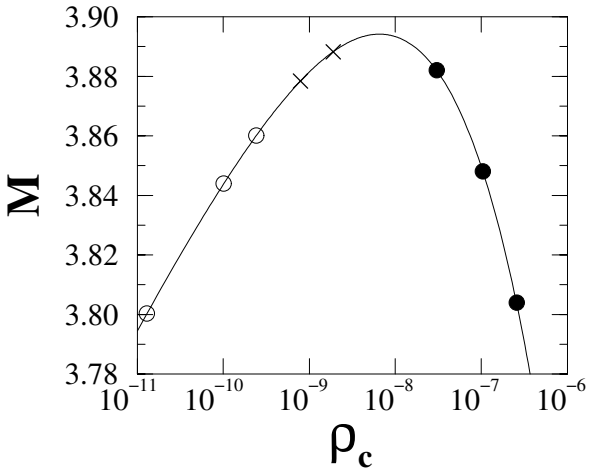

FIG. 1.—Probing the dynamic stability of a spherical SMS with $n = 2.96$. Here, ρ_c is the central density of the equilibrium spherical star. Filled circles and crosses represent unstable stars, while open circles represent stable stars according to our dynamic calculation. A cross indicates that the star is actually stable analytically according to the turning point criterion. The radii of the eight marked stars are $R/M = 150$, 200, 300, 750, 1007, 1499, 2001, and 4003, where the sequence starts at the right side of the figure at the highest central densities. With the adopted grid resolution, our code can distinguish stable from unstable stars to within 1% of the maximum gravitational mass.

Figure 1 is a summary of our stability code calibration for a spherical SMS. We find that with the above grid resolution, our code can distinguish stable from unstable stars to within 1% of the maximum gravitational mass. Figure 2 compares the dynamic behavior of stable and unstable stars. Note that we use the unit of time as $t_D \equiv \left(R_e^3/M\right)^{1/2}$ where R_e is the initial equatorial radius ($R_e = R$ for a spherical case). For dynamically unstable stars the central density increases monotonically, while for stable stars it oscillates.

3.2. *Rotating Case*

To assess the ability of our code to distinguish stable from unstable stars with rotation, we consider an equilibrium sequence of uniformly rotating stars of fixed angular momentum J ($J/M^2 = 0.644$ at the turning point). While the turning point criterion strictly identifies the onset of secular instability (Friedman, Ipser, & Sorkin 1988), the point of onset of dynamic instability nearly coincides with the secular instability point (Shibata, Baumgarte, & Shapiro 2000). We adopt the same polytropic index and grid resolution as in the spherical simulations reported above. We decrease the initial pressure as in the spherical case ($\kappa \rightarrow 0.99\kappa$).

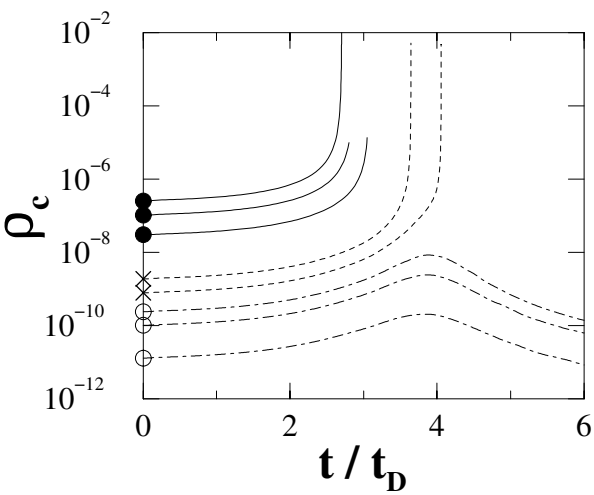

FIG. 2.—Evolution of the central densities of the stars plotted in Fig. 1. Here $t_D = R_e(R_e/M)^{1/2}$, where R_e is the initial equatorial radius. Curves are drawn for stars that are unstable both numerically and according to the turning point criterion (*solid curve*), unstable numerically but stable according to the turning point criterion (*dashed curve*), and stable both numerically and according to the turning point criterion (*dash-dotted curve*).

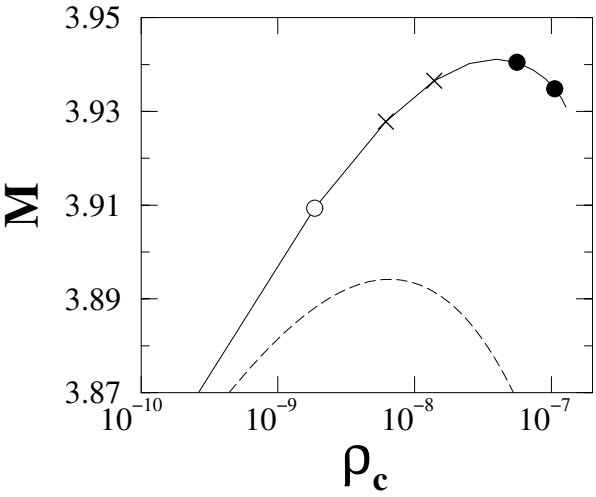

FIG. 3.—Probing the dynamic stability of a rotating SMS with $n = 2.96$, $J = 10$. Circles and crosses have the same meanings as in Fig. 1. The radii of the five marked stars are $R/M = 252$, 285, 419, 537, and 785, where the sequence starts at the right side of the figure at the highest central densities. Note that the solid line shows a constant J sequence with $J = 10$, while the dashed line represents the spherical equilibrium sequence (Fig. 1). With the adopted grid resolution, our code can distinguish stable from unstable stars to within 1% of the maximum gravitational mass.

Figure 3 summarizes our dynamic stability analysis for the rotating SMS. We conclude that with the adopted grid resolution, our code can distinguish stable from unstable rotating stars to within 1% of the maximum gravitational mass. Figure 4 shows the evolution of the central density for stable and unstable rotating stars.

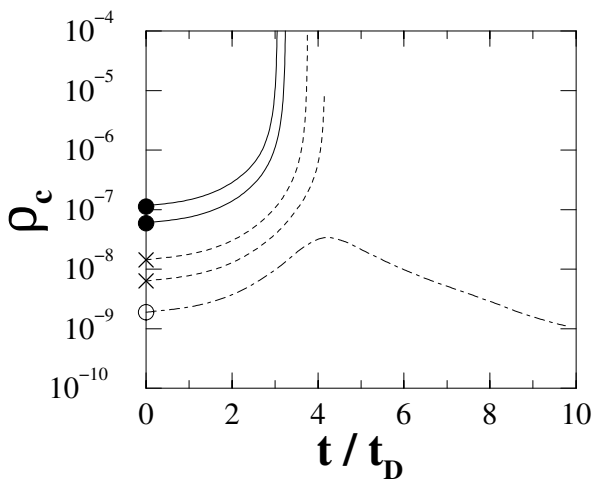

FIG. 4.—Evolution of the central densities of the stars plotted in Fig. 3. Curves are drawn for stars that are unstable both numerically and according to the turning point criterion (*solid curve*), unstable numerically but stable according to the turning point criterion (*dashed curve*), and stable both numerically and according to the turning point criterion (*dash-dotted curve*).

4. CATASTROPHIC COLLAPSE

In this section, we simulate catastrophic collapse, focusing on the possibility of bar formation and on the final fate of the central object. First, we examine spherical SMS collapse in PN hybrid gravitation to verify numerically that we can recover homology over the expected range of radii and that we can resolve the late stages of the collapse as long as general relativistic gravity is not too strong. Next, we examine the collapse of a rapidly rotating $n = 1$ polytrope to check that our code can reproduce bar formation when the collapse is followed by a bounce. Finally, we investigate the collapse of a uniformly rotating SMS, which is the main result of this paper. We discuss the final fate of the SMS collapse, the formation of an SMBH, and the possibility of circumstellar disk formation and mass loss.

4.1. *Spherical Collapse*

We examine spherical SMS collapse to check the range of radii over which homology holds during the collapse in PN hybrid gravitation. For the collapse of an $n = 3$ spherical Newtonian star, self-similarity is strictly preserved (Goldreich & Weber 1980). In full general relativity the collapse of an $n = 3$ spherical star maintains self-similarity down to the radius $R/M \lesssim 80$ (Shapiro & Teukolsky 1979). Therefore, we expect that there is some region over which self-similarity is maintained in PN hybrid gravitation. Because $n = 3$ spherical stars are marginally unbound, the system may expand rather than collapse for this polytropic index when we integrate with finite grid resolution. To guarantee collapse, we choose a slightly lower index, $n = 2.96$, for our computation. Since this computation is only to reconfirm homologous behavior above a minimum stellar radius and to probe how our code signals the final fate of spherical collapse (a BH), we choose a modest initial radius $R/M_0 = 150$. By performing this spherical collapse in three dimensions instead of one dimension, this simulation does provide a useful test bed for our subsequent rotating collapse simulation. The parameters characterizing our initial equilibrium star are summarized in Table 1. We acknowledge that our hybrid PN code cannot accurately handle BH formation, which is a fully general relativistic phenomenon. However, we expect to be able to follow collapse far enough to ascertain whether or not BH formation is the likely outcome.

We plot density profiles for the collapsing star at selected times in Figure 5. We decrease the initial pressure of the equilibrium star by 1% ($\kappa \rightarrow 0.99\kappa$) to induce collapse. We see that the collapse is nearly homologous up to a time $t/t_D \sim 2.5$. The radius at that time is $R/M_0 \sim 80$. Note that the central density exceeds 20 times its initial value at this point. Our result is consistent with that of Shapiro & Teukolsky (1979), who found that homology was maintained until $R/M \sim 80$. We do not expect homologous evolution beyond this point, because of deviations from Newtonian behavior. We continue the collapse to $t = 2.70t_D$, by which time the lapse has decreased to $\alpha_c \sim 0.2$ and the mean radius is about $r_m/M_0 \sim 2.0$ (recall that the horizon radius for a static BH in the adopted isotropic coordinate system is $r/M = 0.5$). Given the plunge in the lapse, we may safely guess that a BH will form after further collapse.

TABLE 1

PARAMETERS FOR THE INITIAL SPHERICAL EQUILIBRIUM SMS

Parameter	Value
$\bar{\rho}_c$	2.56×10^{-7}
$\bar{M}$	3.80
R/M	150

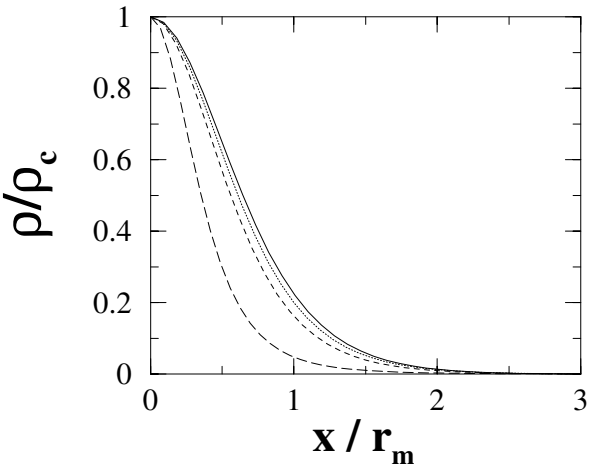

FIG. 5.—Density profiles at selected times during spherical SMS collapse. Solid, dotted, dashed, and long-dashed lines show profiles at $t/t_D = 0$, 2.04, 2.52, 2.68 and $[\rho_c/\rho_c^{(0)}, R/M_0] = (1, 146)$; (3.05, 131); (16.5, 76.0); and (770, 24.8), respectively. Note that when a profile overlaps the solid line, the system is strictly homologous. Homology is maintained in this spherical collapse up to the time at which $R/M_0 \sim 80$.

4.2. *Core Collapse and Bounce*

One scenario that leads to bar formation is core bounce following the collapse of a rotating star. Simulating this phenomenon tests the ability of our code to detect a bar-mode instability. Two previous numerical studies focus on nonaxisymmetric instabilities arising in the core-collapse supernova (Rampp et al. 1998; Brown 2001). The effective Γ in both cases is larger than 4/3 at the time of maximum compression, which causes the bounce. They conclude that once the star exceeds the value $T/W \sim 0.27$, bar formation takes place after several dynamic timescales. We use a similar scenario to test our code by reproducing this result. We adopt a stiff $n = 1$ ($\Gamma = 2$) polytropic model to guarantee a core bounce following a modest decrease in initial radius. Since the change in radius is not large, we do not need to install a scale factor in this calculation. Since core bounce will generate a shock between the infalling and outgoing matter, we must utilize artificial viscosity in our code.

TABLE 2

PARAMETERS FOR THE INITIAL ROTATING EQUILIBRIUM $n = 1$ POLYTROPE

Parameter	Value
$\bar{\rho}_c$	5.00×10^{-3}
$\bar{M}$	1.34×10^{-3}
$\bar{J}$	4.43×10^{-4}
R_p/M	70.4
J/M^2	1.91
T/W	8.18×10^{-2}
R_p/R_e	0.675

The initial data for this case is summarized in Table 2. We choose initial data near the mass-shedding sequence in order to make the initial value T/W as large as possible. We also choose the initial equilibrium star so that the equatorial radius remains in the PN regime, $R/M \gtrsim 20$. In order to achieve an appreciable implosion prior to bounce, we drastically deplete the initial pressure by decreasing κ according to

$$\kappa \rightarrow 0.09\kappa \, . \tag{41}$$

We also impose a slight triaxial density perturbation on the equilibrium star to induce $m = 2$ bar formation (Rampp et al. 1998):

$$\rho = \rho^{(\mathrm{equilibrium})} \left(1 + \delta \frac{x^2 - y^2}{R_e^2} \right) , \tag{42}$$

where $\delta = 0.1$. We employ a grid size ($239 \times 239 \times 120$) that covers the initial equilibrium star with 161 points across the equatorial diameter. In fact, the proper equatorial radius varies between $30 \lesssim R_e/M \lesssim 104$ during the collapse, so the resolution of the central region is always adequate during the evolution.

The bar diagnostics are shown in Figure 6. Our results are similar to those of Rampp et al. (1998), especially the behavior of T/W (Fig. 3 of Rampp et al. 1998). Figure 6 shows the evolution of the nonaxisymmetric distortion function. Its growth signifies bar formation.

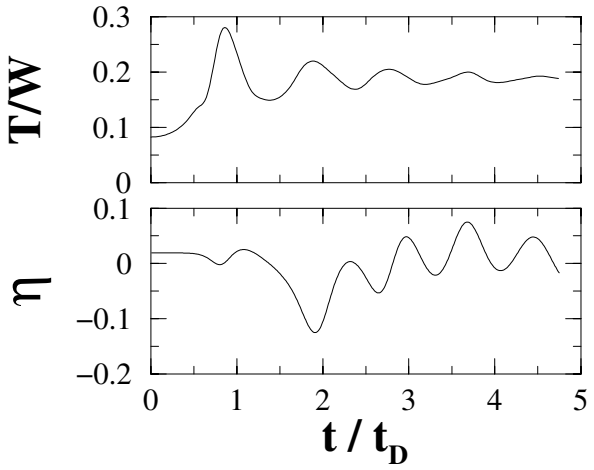

FIG. 6.—Growth of the bar in rotating core collapse and bounce. The quantity T/W exceeds the critical dynamic instability point $\sim$0.27 during the collapse and settles down below this value to $T/W \sim 0.19$. The deformation parameter η grows exponentially during the early evolution following maximum compression and oscillates about a finite value at late times. Note that the behavior of T/W is quite similar to Fig. 3 of Rampp, Müller, & Ruffert (1998).

We plot density contours at selected times in Figures 7 (equatorial plane) and 8 (meridional plane). A modest spiral arm forms within a dynamic time after the star exceeds $T/W = 0.27$ (Fig. 7*b*). After that, the spiral arm is twisted

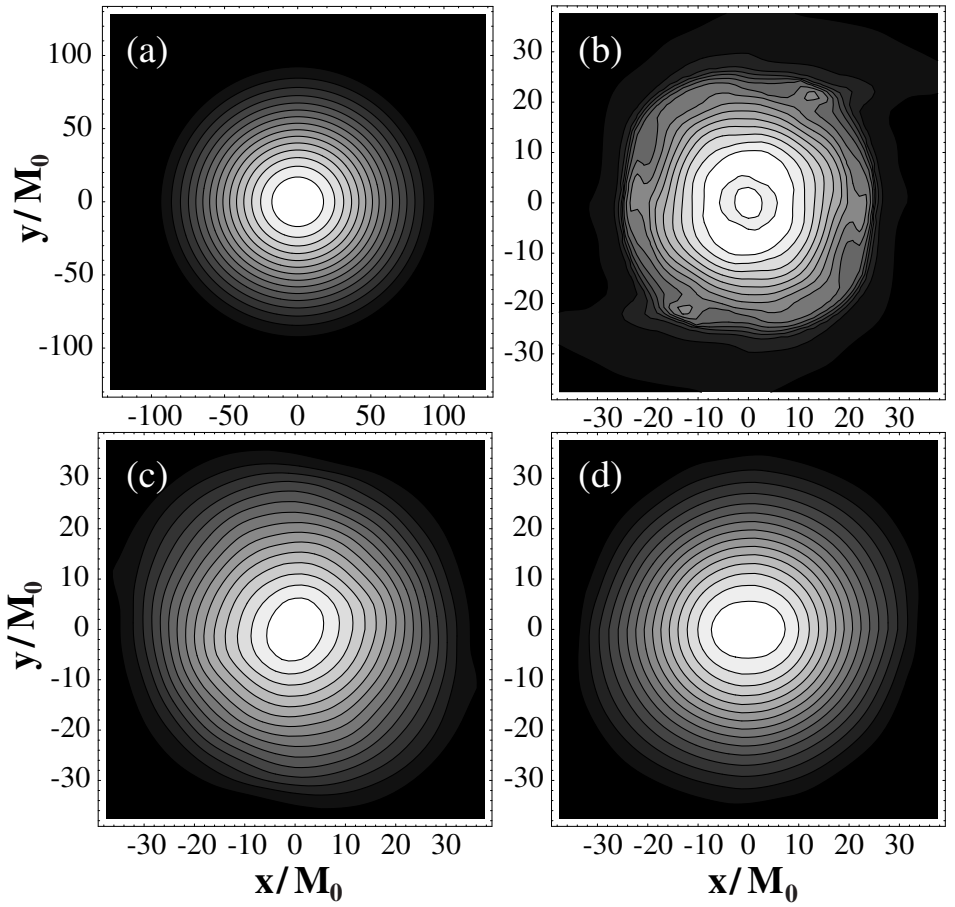

FIG. 7.—Density contours ρ_* in the equatorial plane at selected times during the collapse and bounce of a rotating star. Snapshots are plotted at $(t/t_D, \rho_c^*)$ = (*a*) $(4.90 \times 10^{-5},\ 5.353 \times 10^{-3})$; (*b*) $(1.41,\ 1.410 \times 10^{-1})$; (*c*) $(3.43,\ 1.435 \times 10^{-1})$; and (*d*) $(4.70,\ 1.478 \times 10^{-1})$. The contour lines denote densities $\rho^* = \rho_c^* i/16\,(i = 1,\ \ldots,\ 15)$.

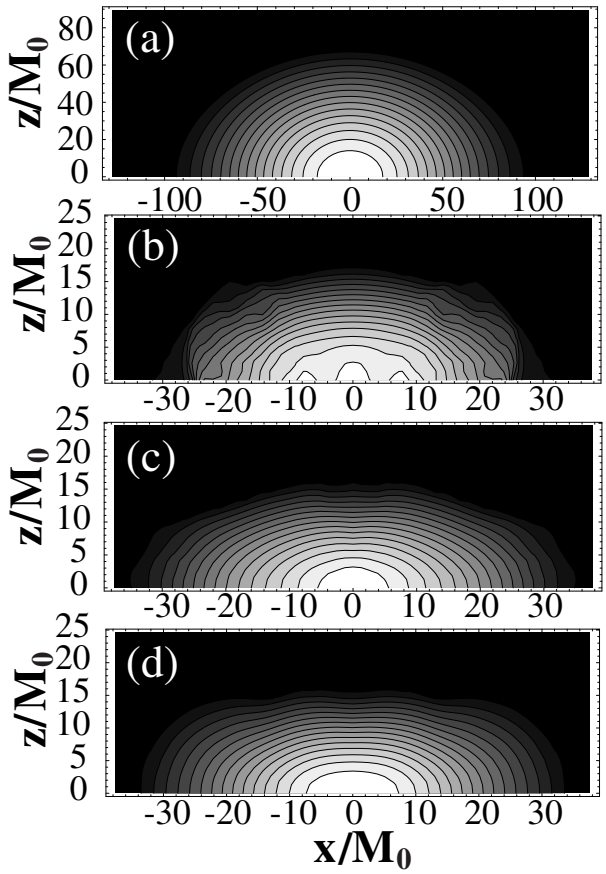

FIG. 8.—Density contours ρ_* in the meridional plane at selected times during the collapse and bounce of a rotating star. The times and contour levels are the same as in Fig. 7.

around the star and settles down to a weakened bar structure at the central core. This whole picture is qualitatively similar to the result reported in Rampp et al. (1998).

From the density snapshots and the behavior of distortion function, we conclude that our code has successfully reproduced (weak) bar formation during core collapse and bounce. We thereby confirm that the code is capable of identifying bars when the physical conditions make it possible for them to form.

4.3. *Rotating SMS Collapse*

Consider an overview of SMS evolution (Baumgarte & Shapiro 1999). Cooling and contraction of a rotating SMS will ultimately spin it up to the mass-shedding limit. After that, the SMS contracts secularly along the mass-shedding sequence as it cools, slowly losing mass and maintaining uniform rotation via viscosity and/or magnetic braking (Zeldovich & Novikov 1967; Shapiro 2000). Upon reaching the onset of radial instability, the star will collapse catastrophically and form a BH, a flattened rotating disk, or some combination thereof. It is this catastrophic collapse that we wish to follow with our dynamic code.

We summarize the parameters of our initial uniformly rotating star in Table 3. We slightly perturb the initial equilibrium state according to

$$\kappa \rightarrow 0.99\kappa\,, \tag{43}$$

$$\rho = \rho^{(\mathrm{equilibrium})}\left(1 + \delta\frac{x^2 - y^2}{R_e^2}\right), \tag{44}$$

where $\delta = 0.1$. We slightly decrease κ in order to deplete the pressure and initiate the collapse. We install a triaxial density perturbation to provide the seed for bar formation if the physical situation should lead to unstable growth. We adopt a grid size ($239 \times 239 \times 120$) so that the star is initially covered by 161 points across the equatorial diameter. We evolve the rotating SMS up to the point at which the PN approximation breaks down.

We show the evolution of the central lapse function in Figure 9. The figures shows that we can follow the collapse from the Newtonian regime where $\alpha_c \sim 0.99$ to the relativistic regime where $\alpha_c \sim 0.3$. The rapid plummet of α_c below 0.3 at late times indicates that a BH will form as an immediate consequence of collapse.

We plot the mass and angular momentum during the evolution in Figure 10. Our hybrid PN scheme conserves M_0, provided that the adopted cutoff density in the ambient atmosphere is negligible[6] and that there is no mass loss from the grid. Our fully relativistic expressions for M and J, on the other hand, are not necessarily conserved in our hybrid

TABLE 3

PARAMETERS FOR THE INITIAL ROTATING EQUILIBRIUM SMS

PARAMETER	VALUE	
	Our Initial Data	Critical Value[a]
$\bar{\rho}_c$	8.00×10^{-9}	7×10^{-9}
$\bar{M}$	4.57	4.57
$\bar{J}$	20.0	20.3
R_p/M	411	427
J/M^2	0.960	0.97
T/W	8.85×10^{-3}	8.99×10^{-3}
R_p/R_e	0.675	0.664

[a] Baumgarte & Shapiro 1999.

[6] In order to regularize the fluid equations near the surface of the star, it is convenient to put an atmosphere in the vacuum. We do this by setting a cutoff density below which ρ^* may not drop. We define the surface of the star to be the place where $\rho^* = \rho_s^* = 10\rho_{\mathrm{cut}}^*$, where $\rho_{\mathrm{cut}}^*/\rho_c^* \approx 10^{-9}$.

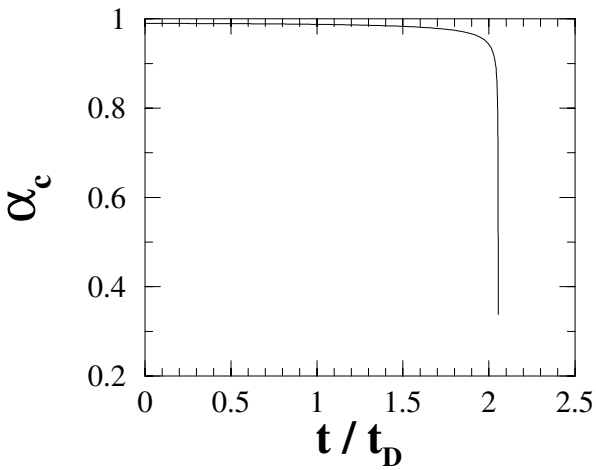

FIG. 9.—Evolution of the central lapse function during rotating SMS collapse.

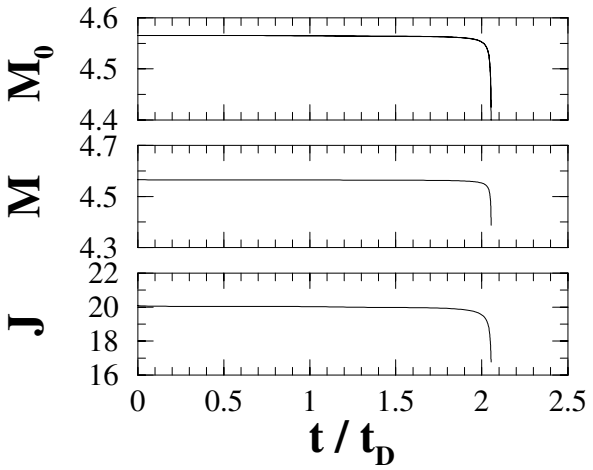

FIG. 10.—Evolution of rest mass M_0, gravitational mass M, and total angular momentum J during rotating SMS collapse. Note that M_0 should be strictly conserved during the evolution within a numerical error, and it is indeed conserved within 4% error (see text).

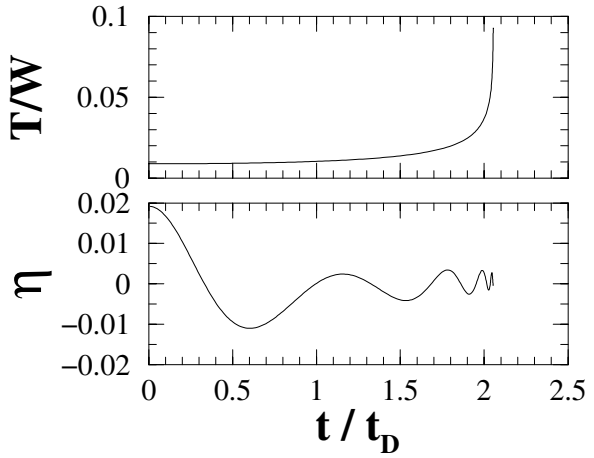

FIG. 12.—Evolution of bar-mode diagnostics during rotating SMS collapse. The deformation parameter η does not grow exponentially even in the final stage.

PN scheme. We therefore choose to normalize all of our length and time units in terms of M_0. Toward the end of our simulation, a small amount (less than 4%) of the matter leaves the computational grid, leading to the loss of rest mass as shown in Figure 10. This figure also demonstrates that M and J are conserved to similar levels, indicating that relativistic effects, which might cause larger deviations, are small. We show the evolution of the scale factor in Figure 11. This plot indicates that the physical grid that we cover shrinks during the collapse from $x_{\max}/M_0 \sim 900$ ($\hat{a} = 1$) to $x_{\max}/M_0 \sim 50$ ($\hat{a} = 0.06$), where $x_{\max}$ is the edge of our numerical grid.

We monitor the bar-mode diagnostics in Figures 12 and 13. The amplitude of the deformation function *decreases* during the evolution, hence we conclude that a nonaxisymmetric bar does not grow prior to BH formation. Even though T/W may exceed ≈ 0.27 in the final stages, there is not sufficient time for growth prior to the appearance of a hole. The reason for the absence of an instability is that T/W does not grow as rapidly as r_m^{-1} during the late stage of collapse, since it would remain spherical (see Fig. 13).

We show the density profile in the equatorial plane in Figure 14 and in the meridional plane in Figure 15. The ability of our scale factor implementation to resolve the matter distribution even as it becomes increasingly compact during the implosion is evident from these snapshots. We find no indication of the formation of a circumstellar disk with significant mass by the termination of our simulation. In fact, the fraction of the rest mass outside a sphere of radius $r/M_0 = 7.0$ is 26% and outside a sphere of $r/M_0 = 28.0$ is 10%. Accordingly, most of the mass is concentrated in the center and is collapsing inward when we terminate our integration. Note that by employing a density cutoff, we are not reliably resolving the very outermost region. However, we note that even with a cutoff, M_0 is conserved to 96% accuracy (Fig. 10). We also note that the overall picture is not affected by a change of the cutoff value or extension of the grid size. We thus conclude that the rotation cannot provide

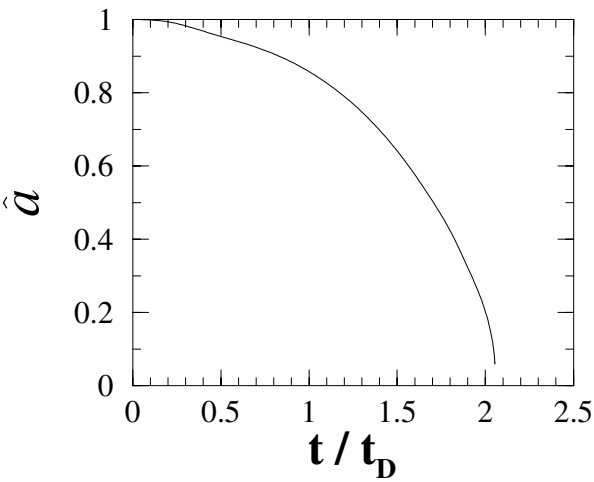

FIG. 11.—Evolution of the scale factor during rotating SMS collapse. The collapse of the scale factor indicates that the physical size of our grid contracts from $R/M_0 \sim 900$ ($\hat{a} = 1$) to $R/M_0 \sim 50$ ($\hat{a} = 0.06$).

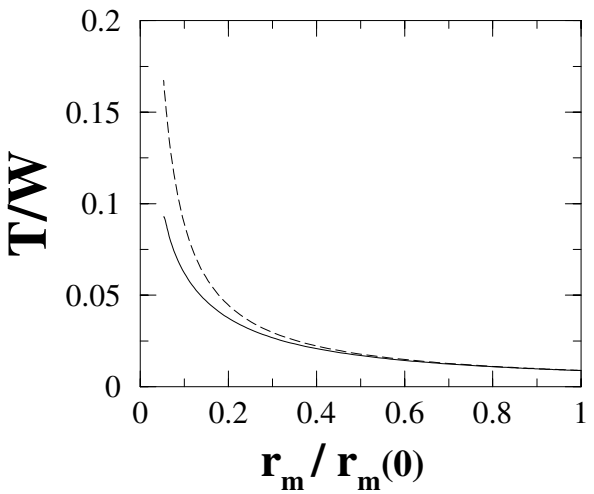

FIG. 13.—Growth of T/W during collapse. The solid line shows the results of our simulation (the same T/W as in Fig. 12). The dashed line assumes $T/W \propto 1/r_m$ during the collapse; this scaling would hold if the collapse were spherical. Note that $r_m(0)$ is the mean radius at $t = 0$.

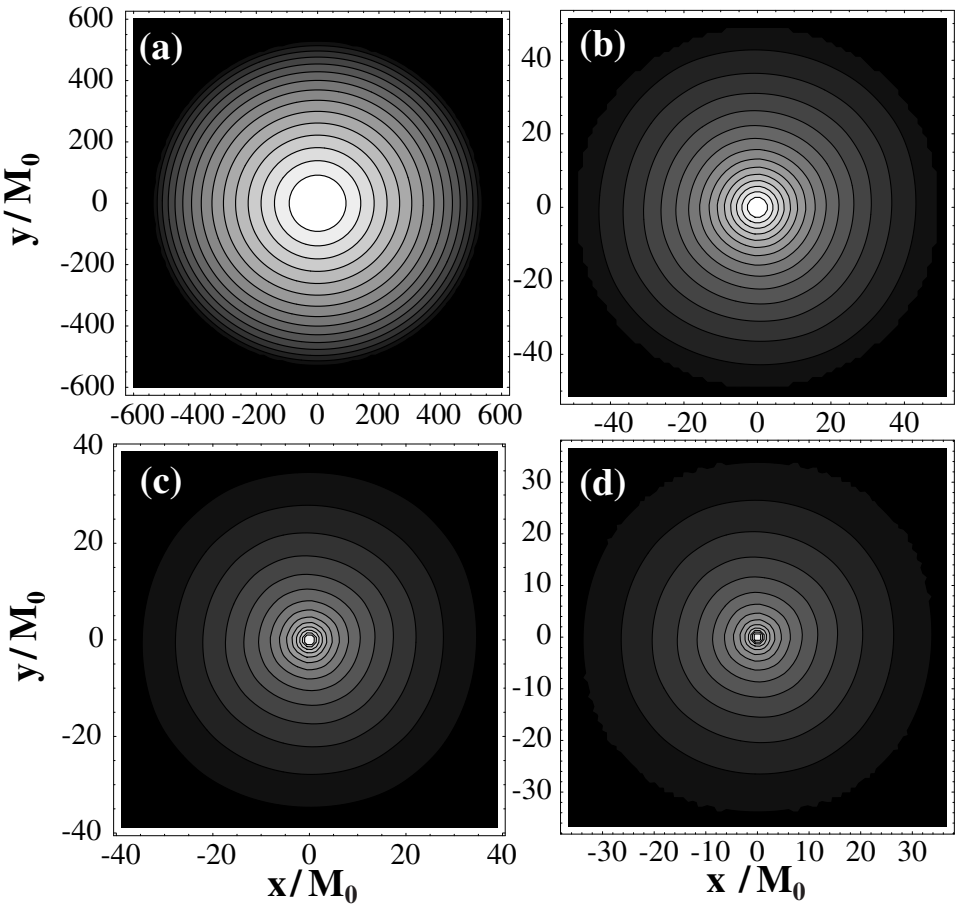

FIG. 14.—Density contours ρ_* in the equatorial plane at selected times during rotating SMS collapse. Snapshots are plotted at $(t/t_D,\ \rho_c^*,\ d) = (a)$ $(5.0628 \times 10^{-4},\ 8.254 \times 10^{-9},\ 10^{-7})$; (b) $(2.50259,\ 1.225 \times 10^{-4},\ 10^{-5})$; (c) $(2.05360,\ 8.328 \times 10^{-3},\ 5.585 \times 10^{-7})$; and (d) $(2.50405,\ 3.425 \times 10^{-2},\ 1.357 \times 10^{-7})$, respectively. The contour lines denote densities $\rho^* = \rho_c^* d^{(1-i/16)}$ $(i = 1,\ \ldots,\ 15)$.

sufficient centrifugal support in the bulk of the envelope to counter gravity and form a significant disk.

Although our computation is terminated when the lapse drops below $\alpha_c \sim 0.3$, we can still infer the final fate of the collapse from examination of the velocity profile of the star (Figs. 16 and 17). The growth of an appreciable inward radial component of the velocity field strongly suggests that immediately after the time we terminate the integrations, the bulk of the matter will cross the event horizon of the nascent BH in a dynamic timescale as measured at the center of the star.

Although the newly formed BH acquires the bulk of the mass in a coherent implosion, it does not obtain all of the mass and angular momentum. Lingering gaseous fragments in the outermost envelope containing negligible mass but nonnegligible angular momentum are not followed in our simulation, which focuses on the imploding massive bulk of the star. These fragments may accrete on a longer timescale (or even escape), but we cannot track their evolution with our current calculation.

Figure 18 shows the angular momentum distribution during the evolution. During the collapse, the central layers begin rotating faster than the surface layers, and the configuration, uniformly rotating initially, acquires appreciable differential rotation.

If all of the initial mass-energy and angular momentum are consumed by the final BH, it will be rapidly rotating with $a/M \approx 1$ (see Table 3). Although we cannot follow the final formation and growth of the BH, our PN simulations suggest that the final a/M may be slightly lower, because of the loss of angular momentum carried by gas orbiting near the equator.

5. DISCUSSION

We follow rotating SMS collapse from the onset of radial collapse at $R_p/M_0 \sim 411$ to the point where the PN approximation breaks down ($R_p/M_0 \sim 8$). The challenge of covering this large a dynamic range is met by introducing a scale factor and a comoving coordinate system that takes advantage of the homologous nature of the initial collapse.

Collapse of a uniformly rotating, relativistically unstable SMS is coherent and leads to the formation of an SMBH containing the bulk of the mass of the progenitor star. It is interesting to contrast our results with those of Loeb & Rasio (1994), who treat the isothermal ($\Gamma = 1$) collapse of initially homogeneous, uniformly rotating, low-entropy clouds via smooth particle hydrodynamics simulations. They find considerable fragmentation into dense clumps and disk formation containing $\sim$5% of the mass. They conclude that a seed BH will form at the center and that it likely will grow gradually by accretion.

We find no evidence of bars prior to BH formation, thus the collapse is largely axisymmetric. As a result, little angu-

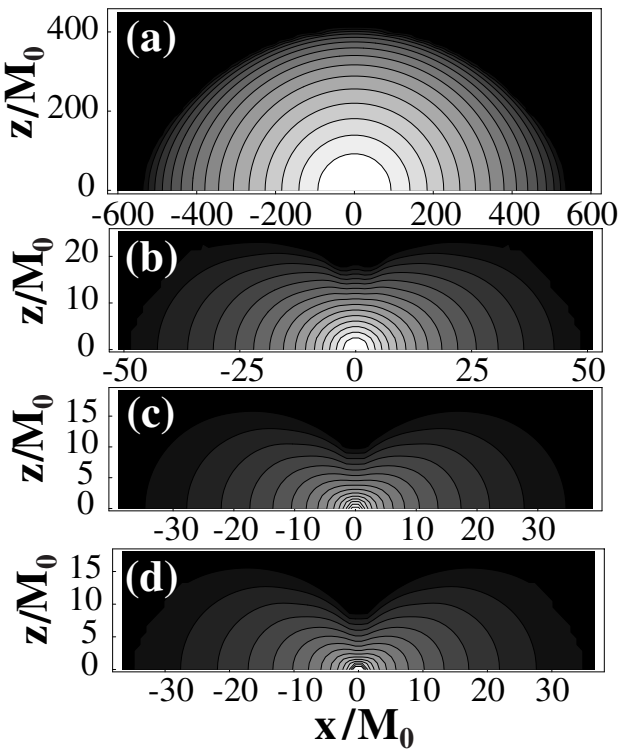

FIG. 15.—Density contours ρ_* in the meridional plane at selected times during rotating SMS collapse. Times, central densities, and contour levels are the same as in Fig. 14.

lar momentum can be radiated away by gravitational waves.

From the coherent, axisymmetric nature of the implosion, we conclude that the collapse of an SMS, rotating uniformly at the onset of collapse, is a promising source of gravitational wave bursts. We can estimate the strength and the frequency of the wave burst emitted from this rotating collapse. The characteristic burst frequency is given by the dynamic timescale of the star at the time of BH formation:

$$f_{\rm burst} \sim \frac{1}{2\pi t_{\rm dyn}} \sim \frac{1}{2\pi}\left(\frac{M}{R^3}\right)^{1/2} = 3\times 10^{-3}\frac{10^6\ M_\odot}{M}\left(\frac{5M}{R}\right)^{3/2}\ ({\rm Hz})\,. \quad (45)$$

The wave amplitude can be estimated by employing the Newtonian quadrupole formula according to

$$h_{\rm burst} \sim \frac{\ddot{Q}}{d} \sim \frac{MR^2 f_{\rm burst}^2}{d} \sim \frac{M}{d}\frac{1}{4\pi^2}\frac{M}{R} = 2\times 10^{-19}\frac{M}{10^6\ M_\odot}\frac{1\ {\rm Gpc}}{d}\frac{5M}{R}\,, \quad (46)$$

where Q is the quadrupole moment of the star and d is the distance from the observer. We set $R/M = 5$, a characteristic mean radius during BH formation. Since the main targets of LISA are gravitational radiation sources between 10^{-4} and 10^{-1} Hz, it is possible that LISA can search for the

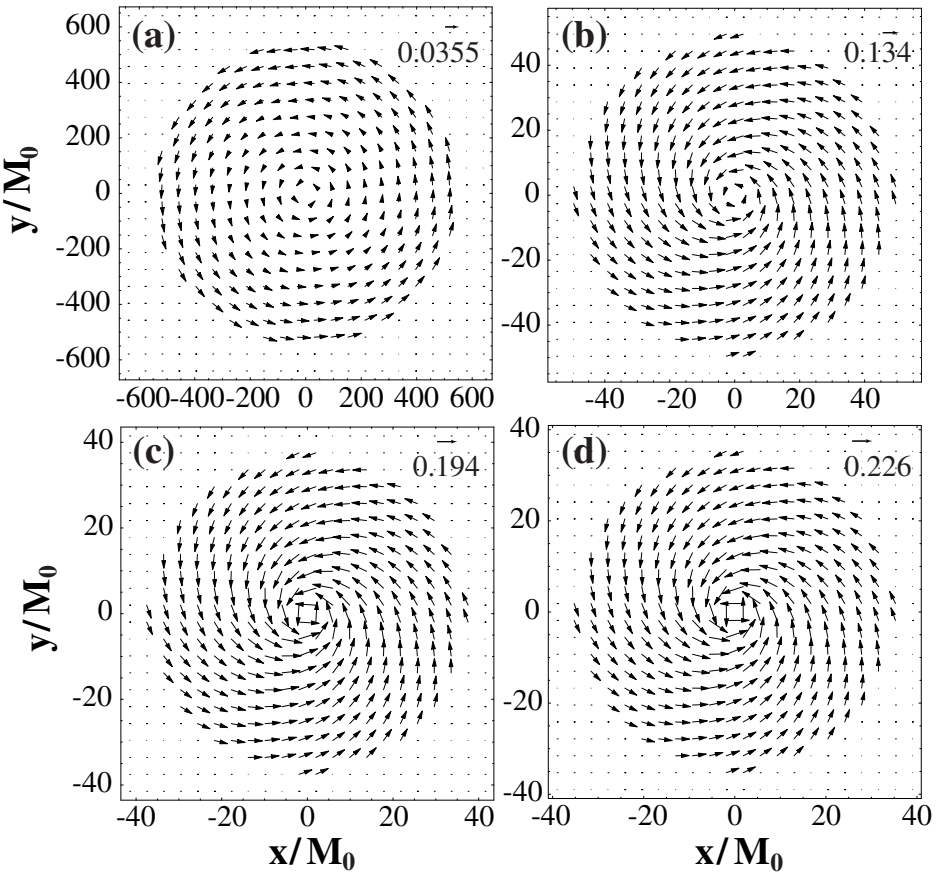

FIG. 16.—Velocity field in the equatorial plane at selected times during rotating SMS collapse. The time for each snapshot is the same as in Fig. 14. Note that the velocity field is drawn in physical coordinates and the velocity arrows are normalized as indicated in the upper right-hand corner of each snapshot.

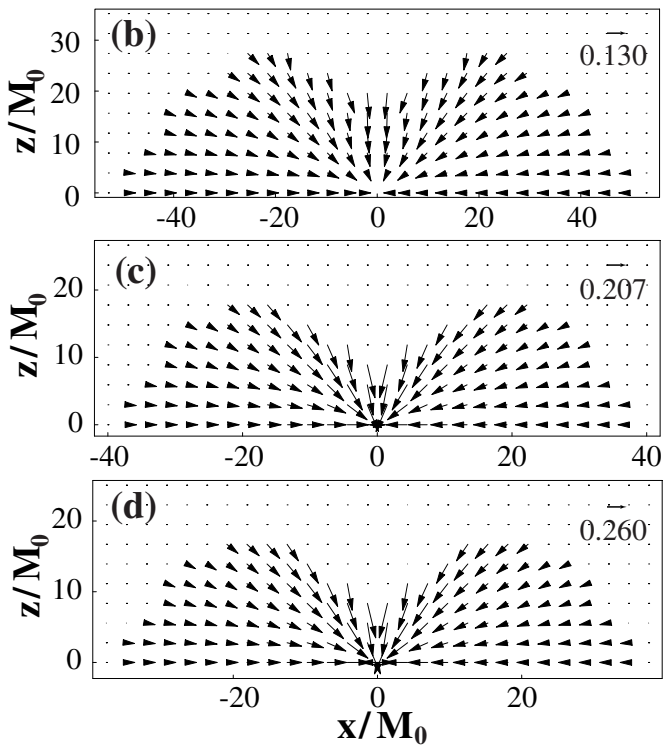

FIG. 17.—Velocity fields in the meridional plane at selected times during rotating SMS collapse. The time for each snapshot is the same as in Fig. 14. We omit Fig. 17*a* because there is no velocity in the meridional plane at $t = 0$.

burst waves accompanying rotating SMS collapse and formation of an SMBH.

In the absence of bar formation, SMS collapse will not produce quasi-periodic waves prior to SMBH formation. Such waves, however, will be generated by the nascent BH via quasi-normal mode ringing. The characteristic frequency $f_{\rm QNM}$ and strength $h_{\rm QNM}$ of this radiation in rotating star collapse are (Thorne 1987; Shibata, Shapiro, & Uryu 2001)

$$f_{\rm QNM} \sim 2 \times 10^{-2} \frac{10^6\ M_\odot}{M}\quad ({\rm Hz})\,, \tag{47}$$

$$h_{\rm QNM} \sim 6 \times 10^{-19} \left(\frac{\Delta E_{\rm GW}/M}{10^{-4}}\right)^{1/2} \left(\frac{2 \times 10^{-2}\ {\rm Hz}}{f_{\rm QNM}}\right)^{1/2} \times \left(\frac{M}{10^6\ M_\odot}\right)^{1/2} \frac{1\ {\rm Gpc}}{d}\,, \tag{48}$$

where $\Delta E_{\rm GW}$ is the total radiated gravitational wave energy. Here we use the $l = m = 2$ quasi-normal mode frequency $\omega_{\rm QNM}$ for a Kerr BH with $a/M = 0.9$, for which $M\omega_{\rm QNM} = 0.7$ (Leaver 1985). The efficiency of the radiated energy could be less than $\Delta E_{\rm GW}/M \lesssim 7 \times 10^{-4}$ for a rotating collapse (Stark & Piran 1985). From the above estimate, gravitational waves from the vibration of a newly formed SMBH reside within the sensitivity limits of LISA.

Since we assume that the equilibrium SMS is uniformly rotating initially, it cannot support a large amount of angular momentum without exceeding the mass-shedding limit. When internal magnetic fields and viscosity are weak, however, the equilibrium star may rotate differentially and support a considerably larger angular momentum (and higher T/W) without exceeding the mass-shedding limit. For such

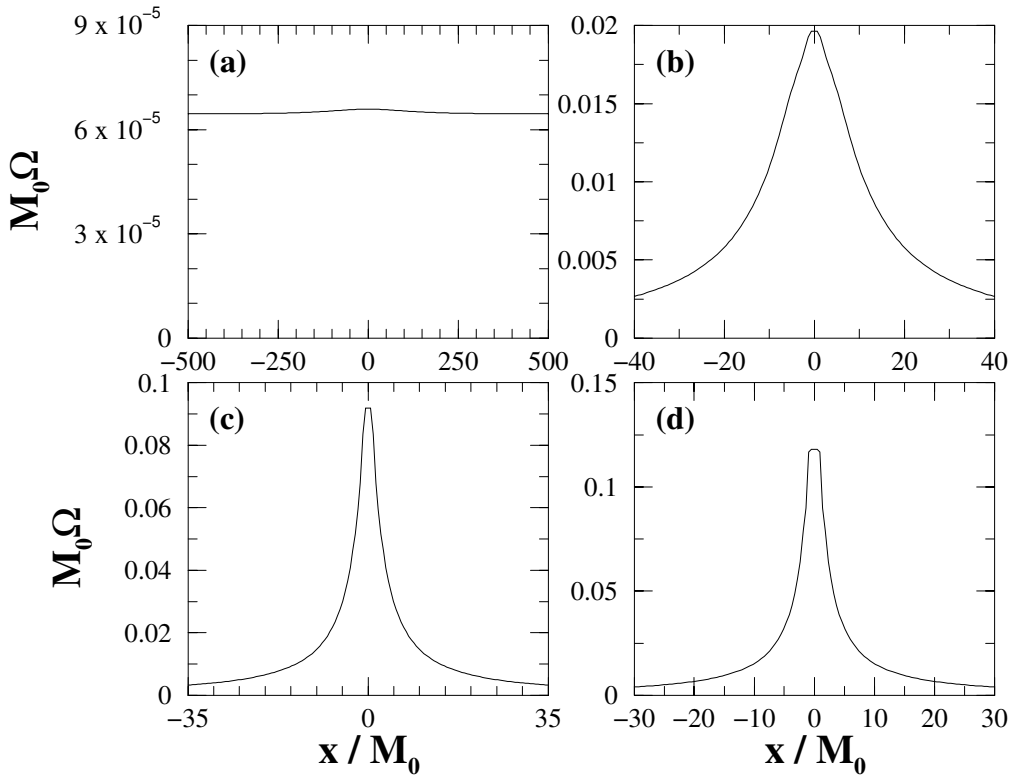

FIG. 18.—Angular momentum distribution along the x-axis at selected times during rotating SMS collapse. The time for each snapshot is the same as Fig. 14.

a case, New & Shapiro (2001) propose an alternative scenario for the quasi-static cooling and contraction of an equilibrium SMS that inevitably leads to bar formation prior to catastrophic collapse. Such a scenario will almost certainly generate long-wavelength quasi-periodic wave emission, even in the absence of SMBH formation.

Our $(3 + 1)$ hybrid PN calculations offer a first glance at SMS collapse. An improved description will require several refinements to our computational scheme. First, it will be necessary to employ a fully relativistic treatment of Einstein's field equations to explore the final dynamic phase of collapse once a BH has formed. In fact, we cannot reliably use PN gravity once the radius decreases much below $R_p/M \lesssim 20$, since the central fields are becoming strong. One possibility would be to use our output when the central fields are beginning to get strong ($\alpha_c \lesssim 0.5$) as initial data for a fully relativistic $(3 + 1)$ code. This would allow us to take advantage of the faster, more robust PN code to handle the Newtonian and PN implosion regime and switch over to a fully general relativistic code for only the final strong-field phase of collapse.

Second, our computation would benefit significantly from nested grid method (see, e.g., Ruffert 1992) to handle the large dynamic range characterizing SMS collapse. We have successfully exploited approximate homology by introducing a scale factor to set up an approximate comoving coordinate system. However, homology breaks down at the center toward the end of the collapse. Moreover, it is difficult to follow the small amount of matter in the equatorial plane that is supported by centrifugal forces while the bulk of the matter collapses. Nested grid method may provide one means of concentrating computational resources on the central region of the star while simultaneously resolving the low-density outermost regions.

We thank Matt Duez and H.-Thomas Janka for their critical reading of our manuscript. The computations reported here were performed under vector computer NEC-SX5 at the Yukawa Institute for Theoretical Physics, Kyoto University. This work was supported in part by NSF grants PHY 00-90310 and 99-02833 and NASA grants NAG 5-8418 and NAG 5-10781 at the University of Illinois at Urbana-Champaign and a Japanese Monbu-Kagakusho grant 13740143.

REFERENCES

Balberg, S., & Shapiro, S. L. 2002, Phys. Rev. Lett., 88, 101301
Balberg, S., Shapiro, S. L. & Inagaki, S. 2002, ApJ, 568, 475
Baumgarte, T. W., & Shapiro, S. L. 1999, ApJ, 526, 941
Begelman, M. C., & Rees, M. J. 1978, MNRAS, 185, 847
Blanchet, L., Damour, T., & Schäfer, G. 1990, MNRAS, 242, 289
Brown, J. D. 2001, in AIP Conf. Proc. 575, Astrophysical Sources for Ground-based Gravitational Wave Detectors, ed. J. M. Centrella (New York: AIP), 234
Chandrasekhar, S. 1964a, Phys. Rev. Lett., 12, 114 (erratum 12, 437)
———. 1964b, ApJ, 140, 417
———. 1965, ApJ, 142, 1488
Ebisuzaki, T., et al. 2001, ApJ, 562, L19
Fowler, W. A. 1964, Rev. Mod. Phys., 36, 545 (erratum 36, 1104)
Friedman, J. L., Ipser, J. R., & Sorkin, R. D. 1988, ApJ, 325, 722
Goldreich, P., & Weber, S. V. 1980, ApJ, 238, 991
Haehnelt, M. G., Natarajan, P., & Rees, M. J. 1998, MNRAS, 300, 817
Iben, I. 1963, ApJ, 138, 1090
Leaver, E. W. 1985, Proc. R. Soc. London A, 402, 285
Lee, H. M. 1987, ApJ, 319, 801
Linke, F., Font, J. A., Janka, H.-T., Müller, E., & Papadopoulos, P. 2001, A&A, 376, 568
Loeb, A., & Rasio, F. A. 1994, ApJ, 432, 52
Macchetto, E. D. 1999, Ap&SS, 269, 269
New, K. C. B., & Shapiro, S. L. 2001, ApJ, 548, 439
Quinlan, G. D., & Shapiro, S. L. 1987, ApJ, 321, 199
———. 1990, ApJ, 356, 483
Rampp, M., Müller, E., & Ruffert, M. 1998, A&A, 332, 969
Rees, M. J. 1998, in Black Holes and Relativistic Stars, ed. R. M. Wald (Chicago: Univ. Chicago Press), 79
Rees, M. J. 2001, in Black Holes in Binaries and Galactic Nuclei, ed. L. Kaper, E. P. J. van den Heurel, & P. A. Woudt (New York: Springer), 351
Ruffert, M. 1992, A&A, 265, 82
Sanders, R. H. 1970, ApJ, 162, 791
Shapiro, S. L. 2000, ApJ, 544, 397
Shapiro, S. L., & Teukolsky, S. A. 1979, ApJ, 234, L177
———. 1985a, ApJ, 292, L41
———. 1985b, ApJ, 298, 34
Shibata, M. 1997, Phys. Rev. D, 55, 2002
———. 1999, Phys. Rev. D, 60, 104052
Shibata, M., Baumgarte, T. W., & Shapiro, S. L. 1998, Phys. Rev. D, 58, 23002
———. 2000, Phys. Rev. D, 61, 044012
Shibata, M., Oohara, K., & Nakamura, T. 1997, Prog. Theor. Phys., 98, 1081
Shibata, M., & Sasaki, M. 1999, Phys. Rev. D, 60, 084002
Shibata, M., Shapiro, S. L., & Uryu, K. 2001, Phys. Rev. D, 64, 24004
Stark, R. F., & Piran, T. 1985, Phys. Rev. Lett., 55, 791
Thorne, K. S. 1987, in 300 Years of Gravitation, ed. S. Hawkings & W. Israel (Cambridge: Cambridge Univ. Press), 330
———. 1998, in Black Holes and Relativistic Stars, ed. R. M. Wald (Chicago: Univ. Chicago Press), 41
Zeldovich, Ya. B., & Novikov, I. D. 1967, Stars and Relativity, transl. E. Arlock, ed. K. S. Thorne & W. D. Arnett (Chicago: Univ. Chicago Press).
Zeldovich, Ya. B., & Podurets, M. A. 1965, AZh, 42, 963 (English transl. 1965, Soviet Astron.–AJ, 9, 742)